communications chemistry

Article

https://doi.org/10.1038/s42004-024-01385-y

Single polyoxometalate-based nanoclusters characterized by infrared absorption nanospectroscopy

Juba Salhi[1,5], Michele Mattera[1,5], Imad Arfaoui[2], Jan Patrick Calupitan[1], Sandra Alves[1], Claire Troufflard[1], Céline Paris[2], Guillaume Izzet[1], Anna Proust[1], David Kreher[3], Guilhem Simon[2], Alexandre Dazzi[4] & Florence Volatron[1]

Bottom-up engineering is a very attractive field. However, the periodic organization of molecules on a solid substrate is challenging, particularly in the selection of the appropriate characterization technique which is suitable for both large area and accurate analysis at the nanoscale. Here, this study demonstrates the unambiguous identification of complex molecular layers by infrared absorption microscopy at the nanometric scale. This technique allowed for the direct observation of the presence of isolated polyoxometalate-based nanoclusters dispersed all over a substrate.

The self-assembly of molecules to develop emergent materials with tailor-made properties is a promising field appealing to a wide scientific community. The possibility to get a precise engineering at the nanoscale by the bottom-up approach, associated with molecular versatility and variety of accessible dimensionalities (from unidimensional to three-dimensional) make this field very promising in multiple applications[1–3]. In this context, the ability to control the properties of materials through surface functionalization with self-assembled functional molecules is a fast-growing field[4–8]. In particular, surface functionalization by organic, metallo-organic or bio-organic porous supramolecular templates gives the opportunity to incorporate guest functional molecules and paves the way towards fine tuning of functional and multifunctional materials for nanoelectronics and spintronics, confined and on-surface reactivity and catalysis, and sensing[9–13]. Scanning probe microscopies, such as Scanning Tunneling Microscopy (STM), remain the most common technique to characterize arrangements and organizations of molecules at the nanoscale. Under ambient conditions, (i.e., solid-liquid interfaces), the lack of chemical characterization by STM limits it to periodically organized supramolecular structures[14–16]. Otherwise, spectroscopic (Raman spectroscopy, UV-visible spectroscopy, X-ray photoelectron spectroscopy,…) or physical techniques (electrochemical, photoluminescence measurements…) are necessary to complement STM results[4,7,17–21]. Nevertheless these techniques tend to operate on a larger scale (at least microscale) than that of STM (nanoscale to a few hundred of nanometers), which might result in significant but unaddressed incongruencies between the nanoscale (supramolecular assemblies) and microscale structures (aggregates, overlayers, grain boundaries…) being probed.

In light of these considerations, there is a clear necessity for the development of an imaging technique capable of accurately depicting the surface subjected to a spectroscopic analysis on a nanoscale level. In this article, we demonstrate that the infrared absorption nanospectroscopy (AFM-IR) gives an unambiguous characterization of the surface feature of an advanced multilayered molecular system, correlating both the micro and the sub-micron structures observed. The AFM-IR combines an atomic force microscopy (AFM) set-up with a pulsed infrared laser to detect the thermal expansion of the molecule under IR absorption that induces a deformation below the AFM tip[22]. It allows to lower the lateral resolution beyond the diffraction limit, and has been commonly used to characterize polymer surfaces and biological targets (cells, tissues, proteins..)[23,24]. Recently, organic monolayers[25,26], individual nanoparticles[27], carbon nanotubes and graphene sheets[28], and single proteins[29], Aβ42 oligomers[30] and DNA molecules[31] have been imaged by AFM-IR. Here, we demonstrate the characterization of a sophisticated molecular assembly made of pyridine-terminated Keggin-type polyoxomolybdates (POM-pyr) linked to the zinc-phthalocyanine (ZnPc) deposited onto a layer of 1,3,5-tris[(E)-2-3,5-didodecyloxyphenyl)-ethynyl]-benzene (TSB-C_{12}) self-organized on highly oriented pyrolytic graphite (HOPG) by AFM-IR. Polyoxometalates are nanometric molecular oxides (general formula $\{M_xO_y\}^{n-}$ or $\{X_pM_xO_y\}^{m-}$ with M = W^{VI}, Mo^{VI}, V^{V},…; X = P^{V}, Si^{IV}, Al^{III},…) with outstanding physical properties and great chemical versatility, widely studied in a large panel of applications in catalysis, biology, medicine, energy storage, information storage etc[32]. In this study, AFM-IR was decisive to characterize the organization for the POM-pyr/ZnPc molecular complex (named hereafter

[1]Institut Parisien de Chimie Moléculaire (IPCM), CNRS, Sorbonne Université, Paris, France. [2]De la Molécule Aux Nano-Objets: Réactivité, Interactions et Spectroscopies (MONARIS), CNRS, Sorbonne Université, Paris, France. [3]Institut Lavoisier de Versailles (ILV), CNRS, Université Paris-Saclay, Versailles, France. [4]Institut de Chimie Physique (ICP), CNRS, Université Paris-Saclay, Orsay, France. [5]These authors contributed equally: Juba Salhi, Michele Mattera.
e-mail: florence.volatron@sorbonne-universite.fr

POM-ZnPc complex) on the surface with a clear IR response of each component (POM-pyr and ZnPc) and led to the detection of isolated molecular complexes randomly dispersed on the surface.

Results and discussion

POM-ZnPc complex preparation

POMs are highly charged molecules, so their handling and fine organization are very difficult due to POM-to-POM electrostatic interactions often leading to the formation of aggregates[33]. Here, their chemical modification was performed to add a pyridyl-terminated organic arm able to coordinate a metalated phthalocyanine, that would drive their insertion into the pores of a 2D supramolecular assembly (Fig. 1). Indeed, such flat aromatic macrocycles with an apical pyridyl ligand have shown to perfectly fit the pores of a honeycomb network made of TSB-C_{12} molecules[17,18,21]. The pyridine-terminated Keggin type polyoxomolybdate was prepared by a previously reported procedure[34,35]: a Sonogashira coupling between the 4-ethynyl-pyridine and the iodoaryle tin derivative $(TBA)_4[PMo_{11}O_{39}SnC_6H_4I]$ (TBA = tetrabutylammonium counter-cations, Fig. 1a).

^1H and ^{31}P NMR, IR and mass spectroscopies and elemental analysis assessed the purity of the compound (see "materials and methods" and Supplementary Figs. 1–2) displaying the formula: $(C_{16}H_{36}N)_4[PMo_{11}O_{39}SnC_{13}H_8N]{\cdot}2H_2O$ (POM-pyr). The coordination with the ZnPc was proved in solution in solvent mixtures (acetonitrile and chloroform or dichloromethane) in order to facilitate the solubilization of both the POM-pyr and the ZnPc. Around 0.5 equivalent of ZnPc was added to an NMR tube containing the POM-pyr in the binary solvent $CD_3CN/CDCl_3$ (30/70). The amount of added ZnPc was limited by its low solubility in organic solvents (the concentration of a saturated solution is 7.35×10^{-4} mol·L^{-1}) and the minimum concentration required for NMR measurements. The addition of ZnPc induced a clear shift (down to 8.31 ppm) and broadening of the doublet at 8.39 ppm in the ^1H spectrum, corresponding to the two aromatic protons the closest to the nitrogen atom (Fig. 2a and Supplementary Data 1).

Note that the aromatic protons in the beta position of the pyridine group (doublet at 7.22 ppm) were also shifted and broadened to a lesser extent. Both typical multiplets of the ZnPc at 9.32 and 8.04 ppm were also impacted in the presence of POM-pyr, proving qualitatively a coordination between the ZnPc and the POM-pyr in solution via the pyridine group. To estimate the complexation constant, UV-visible spectra of the ZnPc were recorded under the addition of successive amounts of POM-pyr (Fig. 2b and Supplementary Data 2). A saturated solution of ZnPc was first prepared in dichloromethane, then small aliquots of POM-pyr in acetonitrile were added step by step. Several isosbestic points appeared on the UV-visible spectrum from addition of 1 equivalent of POM-pyr, proving the formation of another species. Importantly, a control experiment following exactly the same procedure, but without POM-pyr (successive addition of small aliquots of pure acetonitrile), did not lead to the appearance of isosbestic points (Supplementary Fig. 3a). From Hill's graphs plotted around the isosbestic point at 605 nm in the Q band, the stoichiometry 1:1 of the POM-ZnPc complex was confirmed (1 POM-pyr for 1 ZnPc) and an equilibrium constant of about 10^4 was evaluated (Supplementary Fig. 3b)[36].

POM-ZnPc complex deposition

First, a diluted solution of TSB-C_{12} in chloroform (5×10^{-5} mol·L^{-1}) was drop casted on a freshly cleaved HOPG leading to the TSB/HOPG sample. The formation of a bidimensional honeycomb network on HOPG by the

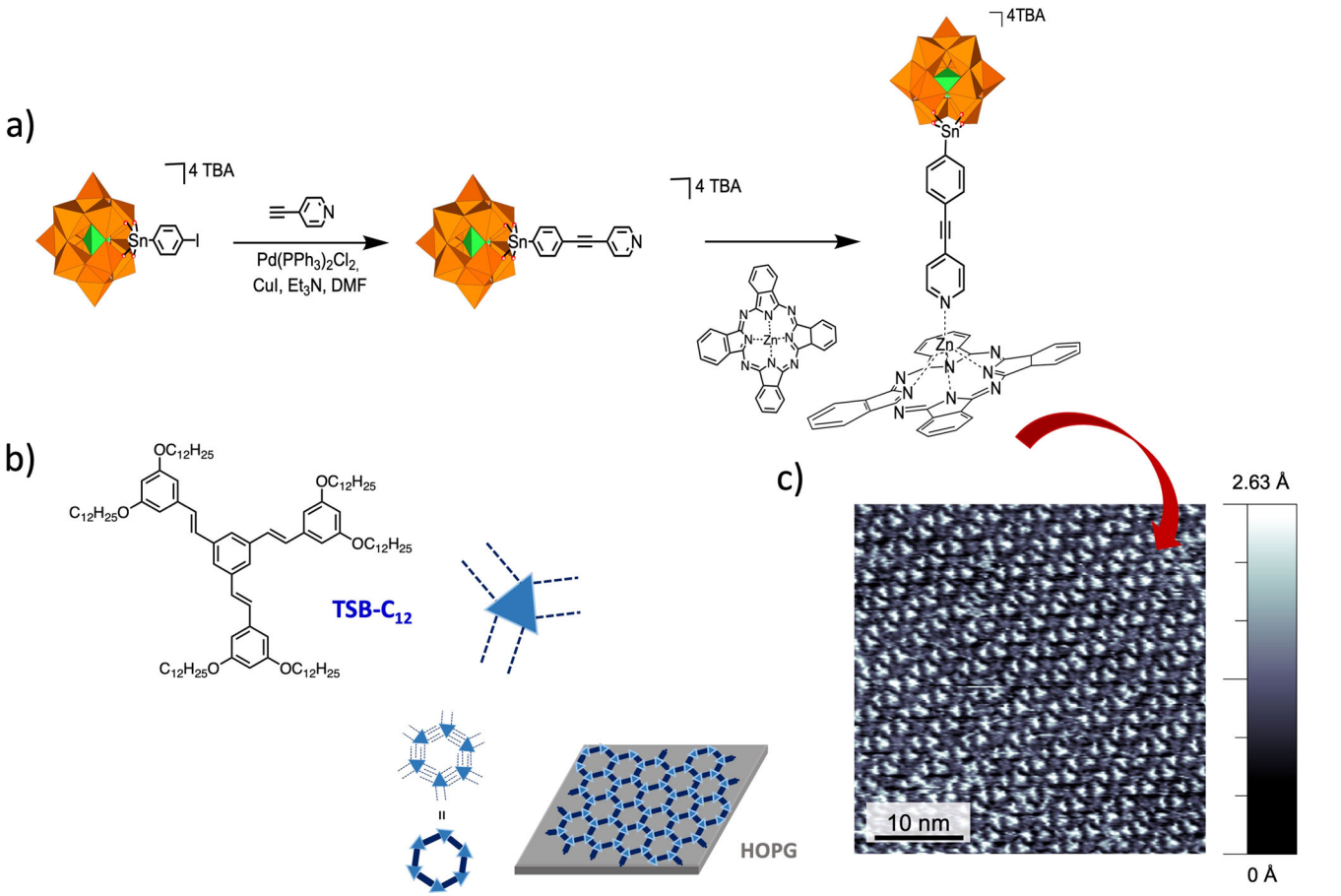

Fig. 1 | Deposition strategy of the POM-ZnPc complex. a scheme of synthesis of the $(TBA)_4[PMo_{11}O_{39}SnC_{13}H_8N]$ (TBA = tetrabutylammonium) and the POM-ZnPc complex; **b** scheme of the TSB-C_{12} and its self-organization on HOPG; **c** STM image of the TSB-C_{12} self-organized on HOPG (50×50 nm^2, solid-phenyloctane interface, I = 30 pA, V = −1V).

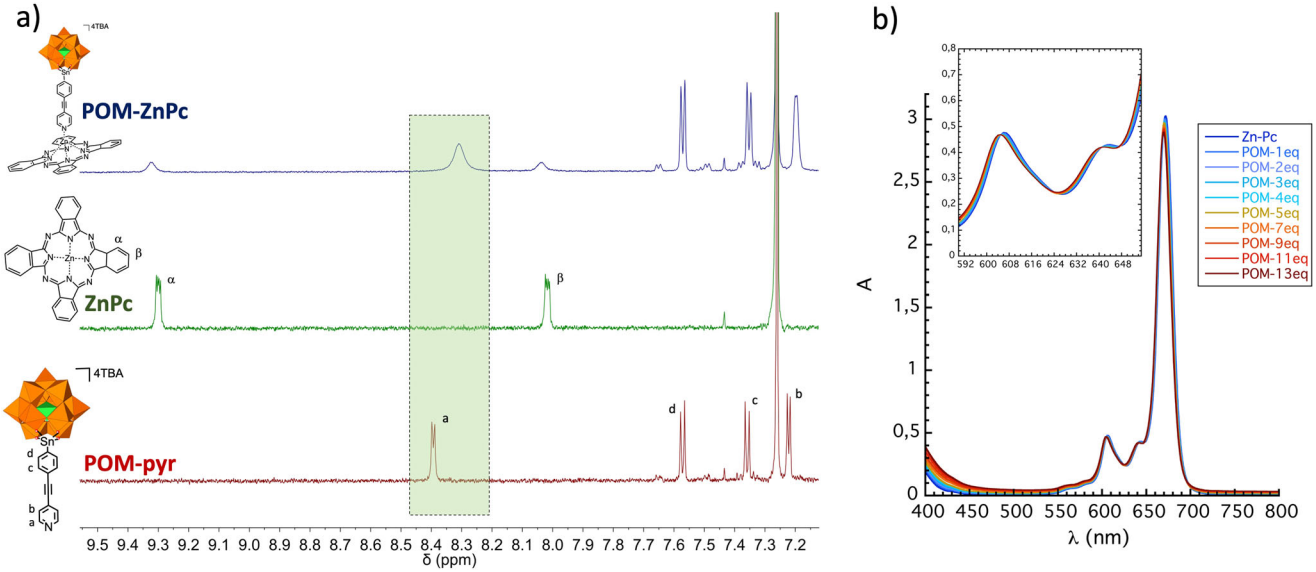

Fig. 2 | Characterization of the POM-ZnPc complex in solution. a NMR spectra in the aromatic area of the POM-pyr (1.3 mmol·L^{-1} in $CD_3CN/CDCl_3$, 30/70, bottom), the ZnPc (0.73 mmol·L^{-1} in $CD_3CN/CDCl_3$, 30/70, middle) and the POM-ZnPc complex (1.3 mmol·L^{-1} of POM-pyr in $CD_3CN/CDCl_3$, 30/70, with 0.5 equivalent of ZnPc, top), a-d refers to the position of the four pairs of equivalent protons of the POM-pyr and their attribution, α and β refers to the position of the two groups of eight equivalent protons of the ZnPc and their attribution; **b** evolution of the UV-visible spectrum of the ZnPc in dichloromethane under addition of small aliquots of POM-pyr in ACN. Insert: zoom of the UV-visible spectra in the 590–655 nm region highlighting the presence of several isosbestic points. From the addition of 5 equivalents of POM-pyr, all the curves were corrected from dilution.

self-assembly of the TSB-C_{12} has already been reported (Fig. 1c)[37]. 20 µL of a solution of the POM-ZnPc complex, prepared by solubilization of 1 equivalent of POM-pyr and 1 equivalent of ZnPc in the binary solvent ACN/$CHCl_3$ (30/70, concentration 1.3×10^{-6} mol·L^{-1}) was then drop-casted on the TSB-C_{12} functionalized HOPG substrate (POM-ZnPc//HOPG sample). To characterize the POM-ZnPc//HOPG sample, we first used a macroscopic characterization technique to identify potential phase segregation on the surface. Raman spectra were recorded on a specific aggregate of the surface using two different excitation wavelengths (Supplementary Fig. 4): at 633 nm, we observed resonance Raman spectrum of the ZnPc, since four typical bands at 747, 1110, 1340 and 1510 cm^{-1} were recorded on the surface sample, corresponding to the lines already reported in the litterature[38]. Moreover, on the same aggregate at 458 nm, the typical bands of the POM-pyr were observed, especially the one at 2225 cm^{-1}, which we assume corresponds to the carbon-carbon triple bond of the organic arm. Both components of the complex were detected on the same aggregate, ruling out the hypothesis of phase segregation during the drying process. However, due to very low concentration, the technique was not sensitive enough to detect any signal on the flat zones. We thus performed STM to examine the POM-ZnPc//HOPG sample, and compared it with the ZnPc deposited on the TSB-C_{12} self-assembled on HOPG (ZnPc//HOPG sample) at a concentration of 1.53×10^{-6} mol·L^{-1} in chloroform. This comparison was undertaken to facilitate the interpretation of the STM images. STM image of the POM-ZnPc//HOPG sample, whatever the tunneling conditions, showed periodically organized nano-objects with a high coverage and a height of approximately 0.6 nm. However, the same images were obtained with the ZnPc//HOPG sample (Supplementary Fig. 5). Note that we obtained similar images with an excess of POM-pyr in the solution of deposition (10 equivalents of POM-pyr for one equivalent of ZnPc) or even by the deposition of a pure POM-pyr solution on the ZnPc//HOPG sample. One can formulate several hypotheses to explain this result: (i) there were phase segregation at the nanometric scale and only the ZnPc were deposited into the pores, the POM-pyr forming aggregates beside; (ii) the POM-ZnPc complexes were integrally deposited into the pores but the STM tip, that was subjected to strong electric fields, was able to interact with the charged POMs and removed them from the surface during the scanning process[39].

AFM-IR characterization

AFM-IR spectroscopy displays several advantages: (1) scanning with a neutral tip while keeping: (2) a nanometric resolution, and (3) a simultaneous recording of the infrared spectrum of the nano-objects on the surface. First of all, the TSB-C_{12} layer on HOPG was characterized. To validate the compatibility of the substrate and the solvent with the AFM-IR technique, a reference spectrum was recorded on the HOPG substrate dedicated to deposition with a drop of chloroform (Supplementary Fig. 6). The spectrum is almost flat with a few bands with very low intensity, probably due to automatic mathematical spectra handling errors. Topography images of the AFM-IR recorded on the TSB/HOPG sample showed a very thin, flat and homogeneous film on large areas (more than several hundreds of microns, Fig. 3a), since the HOPG surface asperities (sheets) were still visible on the image.

Some thick areas, visible with the optical microscope and due to matter accumulation during the drying process of the casted drop (Supplementary Fig. 7) were also imaged (Fig. 3b) and showed thicker films with numerous aggregates with a size of around 20–30 nm. IR spectra were measured both on the thin and thicker areas between the aggregates (Fig. 3c, Supplementary Fig. 8 and Supplementary Data 3). The main characteristic bands of the TSB were recovered on each spectrum, and well reproduced by DFT (Supplementary Fig. 9). Interestingly, the relative intensities of the bands differed between the macroscale (powder recorded with a KBr pellet) and nanoscale (by AFM-IR) measurements. The differences were more pronounced with the thin areas, evidencing that these are due to orientation effects. Indeed, the intensities of the out-of-plane vibration bands at 961, 1389 and 1460 cm^{-1}, perpendicular to the plane of the self-assembly were exalted because of the out-of-plane polarization of the laser illumination. IR images recorded at 1600 cm^{-1} (Fig. 3a, b) confirmed that the TSB-C_{12} was present all over the HOPG surface in the very homogeneous thin areas and that the aggregates in the thick areas were due to TSB-C_{12} molecules aggregations.

To define the characteristic bands of the ZnPc that can be detected by AFM-IR, the ZnPc//HOPG sample was prepared as described above. The film was still very flat and homogeneous at this second step according to the topographic images (Supplementary Fig. 10). On the IR spectrum, the main bands of the TSB-C_{12} were observed except for one band at 1645 cm^{-1},

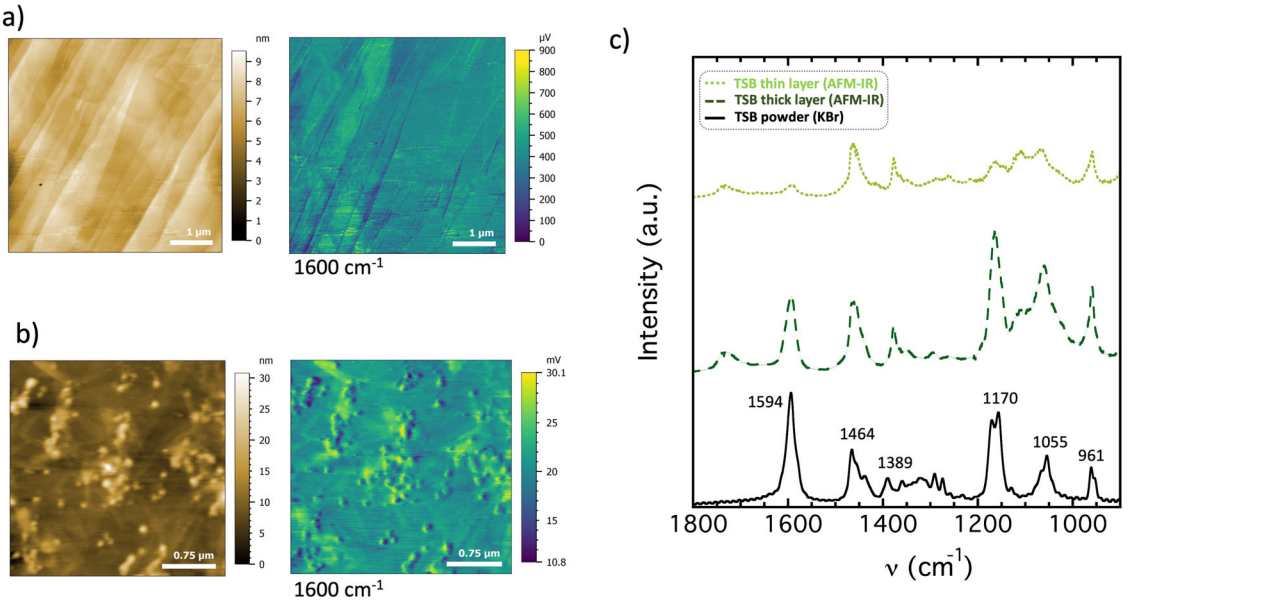

Fig. 3 | AFM-IR characterization of the TSB-C_{12} underlayer. AFM-IR images of the TSB/HOPG sample on (**a**) a flat area, (**b**) a thick area. Topographic images are on the left and IR images recorded at 1600 cm^{-1} are on the right; **c** compared spectra of the TSB powder (FTIR, bottom), the TSB/HOPG sample on a thick area (AFM-IR, average spectrum on 3 spectra, middle), the TSB/HOPG sample on a thin area (AFM-IR, average spectrum on 6 spectra, top). For the sake of clarity, the average AFM-IR spectra intensities were divided (by 10 for the thick layer, 5 for the monolayer). The AFM-IR spectra measured at several locations of the IR images are reported in the Supplementary Fig. 8.

corresponding to a benzene stretching vibration band in the ZnPc. The IR image recorded at this specific wavenumber (1645 cm^{-1}) proved the homogeneous repartition of the ZnPc on the substrate.

Finally, the POM-ZnPc//HOPG sample was measured. Note that, according to the reference samples results, the bands of each component of the complex should be clearly identified from each other and from the bands of the $TSBC_{12}$ (Supplementary Fig. 11): the band at 1645 cm^{-1} for the ZnPc and the characteristic bands at 950, 1034 and 1061 cm^{-1} for the POM-pyr, corresponding respectively to the stretching vibration of the molybdenum-terminal oxygen double bonds and the splitted stretching vibrations of the central phosphorous-oxygen bonds[40]. The topographic image revealed nano-objects of various sizes on the substrate (Fig. 4a). Three types of nano-objects were observed: "big", flat, and small nano-objects.

To determine their nature, we recorded IR images at 950 and 1645 cm^{-1}, which allowed to localize the POM-pyr and the ZnPc components (Fig. 4b, c). Also, IR spectra were registered by focusing on specific nano-objects (Fig. 4d, e, Supplementary Data 3). From the IR images, one can observe that most of the big objects absorbed at 950 and 1645 cm^{-1}, proving that they were made of both POM-pyr and ZnPc. This was confirmed by the spectrum measured on one specific aggregate (marked with a purple line) in which the typical bands at 950, 1034 and 1061 cm^{-1} of the POM-pyr, as well as the benzene stretching band of the ZnPc were detected. They were around 10 nm height, and could correspond to an aggregation of 5 POM-ZnPc complexes (Fig. 4d and Supplementary Data 3). A scheme of the various types of nano-objects is proposed in the Supplementary Fig. 12. One "big" nano-object of the topographic image (marked with a white arrow) was made of pure POM-pyr: it was visible on the IR image recorded at 950 cm^{-1} but not on the IR image recorded at 1645 cm^{-1} (Fig. 4a–c and Supplementary Fig. 12a). The flat nano-objects were large and thin (thickness of around 2 nm) and were made of pure ZnPc, as they were visible only on the IR image recorded at 1645 cm^{-1} and only this band was detected in the IR spectrum (Figs. 4a–c, e and Supplementary Fig. 12b). Interestingly, the ZnPc was also present all over the surface. Indeed, on the IR image recorded at 1645 cm^{-1}, between the aggregates, the absorbance was around 3 mV, proving the presence of a very thin layer of ZnPc absorbing at this wavelength in the background. Thus the flat aggregates corresponded to over layers of ZnPc. It is worth noting that on the contrary, the absorbance was close to zero on the IR image recorded at 950 cm^{-1}, meaning that no POMs were present in the background, as seemed to show the STM images. A 3D image, made of the combination of the topographic image and both IR images allowed an easy visualization of the surface feature: the presence of the pure POM-pyr aggregate (in blue), pure ZnPc aggregates (in red) were clearly visible and all the purple aggregates were made of a mix of both components (Fig. 5a).

Overall, on the image, on the total amount of nano-objects, 28% corresponded to big aggregates made of POM-ZnPc complexes, 1% corresponded to big aggregates made of pure POMs, 6% corresponded to flat aggregates made of pure ZnPc and 65% were small nano-objects. Most of the small nano-objects (55%) appeared in purple in the 3D image. The others (10%) appeared in red, showing the presence of small nano-objects made of limited aggregation of pure ZnPc (Supplementary Fig.12c). For the small purple nano-objects, the IR bands of the ZnPc and the POM-pyr were both present in the IR spectrum recorded on a single object. The height of these nano-objects was around 1.5 nm and the full width at half maximum (FWHM) around 50 nm (Fig. 5b and Supplementary Data 3). It is worth noting that all the small purple nano-objects on this image had this specific FWHM with variable height (between 1.8 and 3 nm) and that the same observation was done on another area of the sample (see Supplementary Fig. 13). A systematic analysis of the size of the nano-objects in the topographic image showed a linear variation of the diameter as a function of the height of the nano-objects (Supplementary Fig. 13e). We thus assumed that the aggregation process was isotropic and that the nano-objects with a FWHM at around 50 nm and a height between 1.8 and 3 nm corresponded to single POM-ZnPc complexes. Theoretically the height of the POM-ZnPc complex is expected between 2.5 and 3 nm, depending on the position and expansion of the TBA counter-cation (Supplementary Fig. 12c). The variation of the height of the nano-objects on the surface should correspond to variable orientation of the POM-pyr versus the ZnPc pedestal through the Zn-N bond. Moreover, if the measurement of the height of the nano-objects is

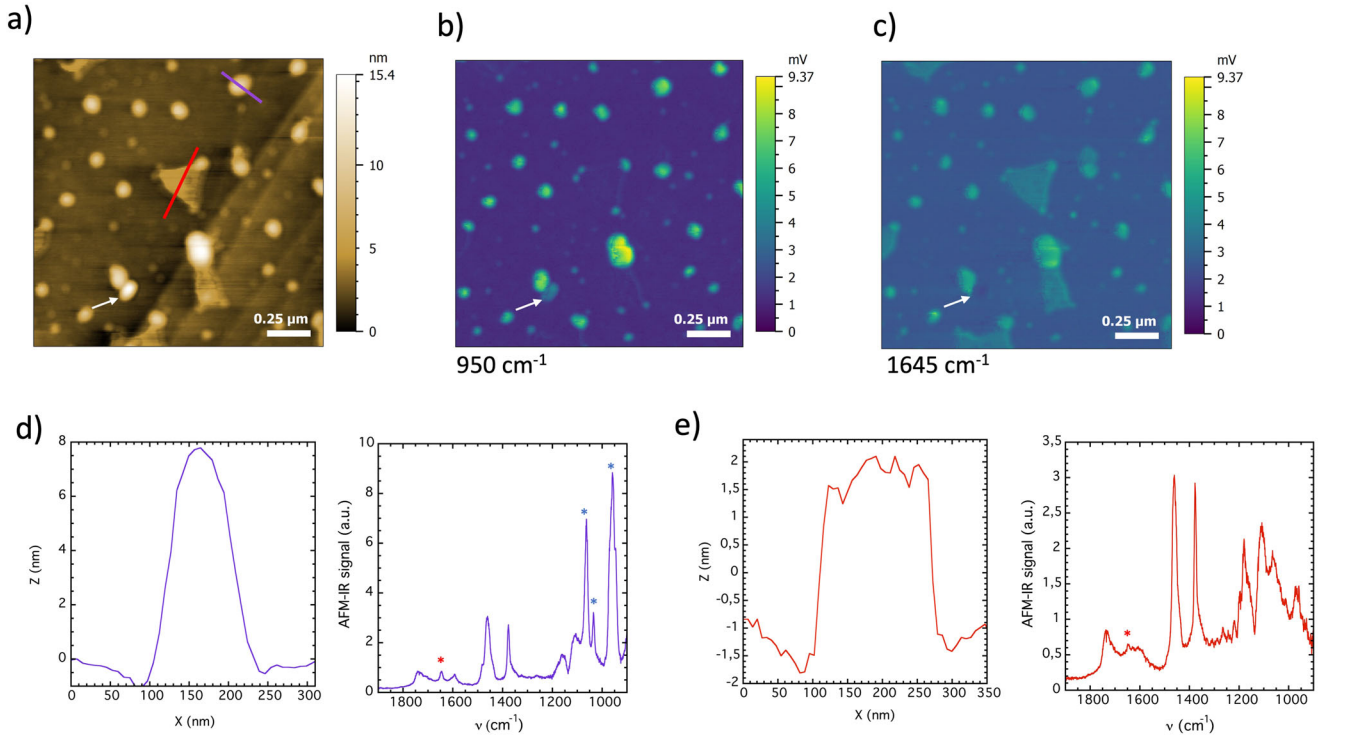

Fig. 4 | AFM-IR characterization of the POM-ZnPc layer. a AFM-IR topographic image of the POM-ZnPc//HOPG sample; **b** AFM-IR infrared image of the POM-ZnPc//HOPG sample recorded at 950 cm^{-1}; **c** AFM-IR infrared image of the POM-ZnPc//HOPG sample recorded at 1645 cm^{-1}; **d** height profile (left) and IR spectrum (right) of a mixed aggregate ("big" nano-object, marked by purple line in the topographic image); **e** height profile (left) and IR spectrum (right) of a pure ZnPc aggregate (flat nano-object, marked by red line in the topographic image). The pure POM-pyr aggregate is marked by a white arrow on the three images.

very accurate with AFM-IR, a lateral distortion is expected due to a deconvolution effect with the tip. A FWHM of around 50 nm is coherent with a tip radius below 50 nm and a lateral size of nano-objects around 1.5–2 nm. Thanks to AFM-IR characterization, we proved the presence of a majority of isolated single POM-ZnPc complexes randomly deposited in the pores of the $TSBC_{12}$ and with variable orientations.

Conclusion

We used AFM-IR to fully characterize an advanced molecular system made of a layer of a POM-ZnPc complex deposited onto a layer of $TSBC_{12}$ self-assembled on HOPG. In contrast to the ZnPc alone, the POM-ZnPc complex tends to form aggregates, probably due to the electrostatic interactions between the charged molecules. ZnPc was observed to insert into the pores of the network formed by $TSBC_{12}$ molecules, as evidenced by STM. However, it was also found to form larger aggregates, which was consistent with the Raman study.

In addition to corroborating the findings of other techniques, AFM-IR yielded a particularly noteworthy result: single POM-ZnPc complexes exhibited a tendency to insert into the pores of the TSB-C_{12} template, in a random manner, occupying isolated locations. In this study, STM was insufficiently sensitive to detect nano-objects distanced of 50–100 nm from each other. Furthermore, it is likely that the individual molecules, which are electrically charged, would interact with the STM tip, which is crossed by a huge electrical field. The use of AFM-IR proved that the hybrid POM preparation strategy, even though it does not guarantee their periodic organization, offers a promising approach to control surface handling of the nanoclusters. In this study, AFM-IR emerged as a crucial technique, with the potential to become a preferred method for the characterization of complex molecular layers.

Materials and methods

All chemicals and solvents were purchased from Merck, Fisher Scientific and VWR and used as received except for triethylamine that was distilled from CaH_2. The $TBA_4[PMo_{12}O_{39}\{Sn(C_6H_4)I\}]$ (TBA = tetrabutylammonium) was prepared as described elsewhere[35]. HOPG substrates were purchased from MaTeck.

Synthesis of $(TBA)_4[PMo_{11}O_{39}SnC_{13}H_8N]\cdot 2H_2O$ (POM-pyr)

$TBA_4[PMo_{12}O_{39}\{Sn(C_6H_4)I\}]$ (200 mg, 0.067 mmol), 4-ethynylpyridine hydrochloride (20 mg, 0.143 mmol), $Pd(PPh_3)_2Cl_2$ (7.3 mg, 0.01 mmol) and CuI (3.2 mg, 0.017 mmol) were solubilized in 4 mL of anhydrous DMF preliminary degassed with argon. Then triethylamine (50 µL, 0.378 mmol) was added and the mixture was stirred overnight. 20 mL of diethylether were added to the solution and the dark solid recovered by centrifugation was dissolved in a minimum of acetonitrile. 20 mL of dichloromethane containing 300 mg (0.936 mmol) of TBABr were added to the solution and the mixture was stirred during 5 min, then centrifuged during 10 min to eliminate the undesirable solid residue. The supernatant was concentrated at the rotary evaporator, precipitated by addition of ethanol, centrifuged, washed twice with 25 mL of ethanol and solubilized in 5 mL of acetonitrile. To remove any presence of protons, 0.081 mmol were taken from a 1 M solution of TBAOH in methanol and diluted 40 times in acetonitrile, then added slowly to the solution containing the POM. After 5 min of stirring, 20 mL of dichloromethane containing 300 mg of TBA (0.94 mmol) were added. This solution was washed 3 times with 40 mL of distilled water, then addition of an excess of diethyl ether to the organic phase allowed the precipitation of a yellow-greenish powder, dried 2 h under vacuum (yield 61%).

^{1}H NMR (300 MHz, CD_3CN):δ (ppm) 8.6 (m, 2H Ar-H), 7.73 (d+dd, $^3J_{H\text{-}H}$ = 8 Hz, $^3J_{Sn\text{-}H}$ = 47.7 Hz, 2H, Ar-H), 7.63 (d+dd, $^3J_{H\text{-}H}$ = 8 Hz, $^4J_{Sn\text{-}H}$ = 16.5 Hz, 2H, Ar-H), 7.47 (m, 2H Ar-H), 3.14 (m, 32H, N-*CH_2*-CH_2-CH_2-CH_3), 1.64 (m, 32H, N-CH_2-*CH_2*-CH_2-CH_3), 1.4 (sex, $^3J_{H\text{-}H}$ = 7.2 Hz, 32H, N-CH_2-CH_2-*CH_2*-CH_3), 0.99 (t, $^3J_{H\text{-}H}$ = 7.2 Hz, 48H, N-CH_2-CH_2-CH_2-*CH_3*); ^{31}P NMR (121 MHz, CD_3CN):δ (ppm) −2.45 (s + d, $^2J_{Sn\text{-}P}$ = 22.2 Hz); IR (KBr pellet, cm^{-1}): ν = 2963 (m), 2934 (m), 2873 (m), 1633 (w), 1594 (w), 1483 (m), 1381 (w), 1062 (s), 1035 (s), 943 (vs), 867 (vs), 807

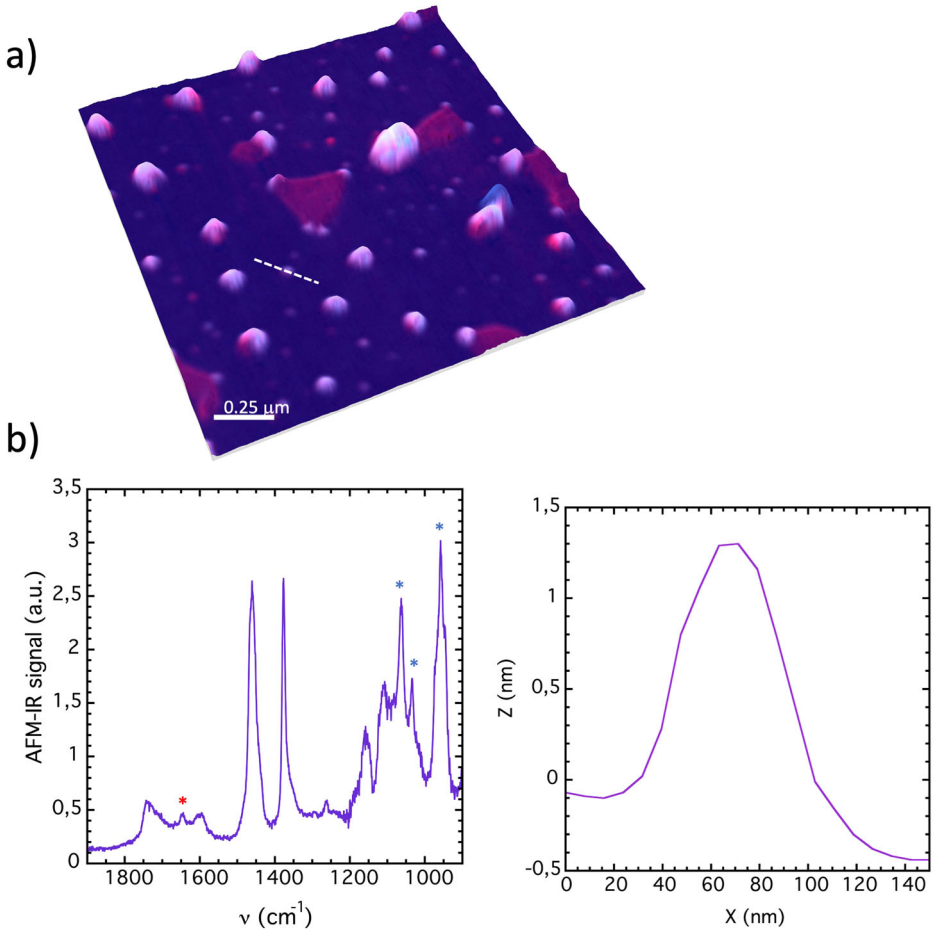

Fig. 5 | AFM-IR analysis of the smallest nano-objects. a 3D AFM-IR image combining topography, IR absorption at 1645 cm^{-1} (red contribution) and IR absorption at 950 cm^{-1} (blue contribution). Absorption at both wavenumbers appears in purple; **b** AFM-IR spectrum (left) and height profile (right) of a small nano-object (marked with white dashes on the 3D image).

(vs), 787 (vs); HRMS (ESI^-): *m/z*: calcd for $PMo_{11}O_{39}SnC_{13}NH_9$: 669.24 $[M+H]^{3-}$; found 669.24 (100); calcd for $PMo_{11}O_{39}SnC_{29}N_2H_{45}$: 1125.50 $[M+H+TBA]^{2-}$; found 1125.50 (100); calcd for $PMo_{11}O_{39}SnC_{45}N_3H_{80}$: 1245.64 $[M+2TBA]^{2-}$; found 1245.64 (12); calcd for $PMo_{11}O_{39}SnC_{29}N_2H_{44}$: 749.66 $[M+TBA]^{3-}$; found 749.66 (5) Anal. Calcd for $(C_{16}H_{36}N)[PMo_{11}O_{39}SnC_{13}H_8N]\cdot 2H_2O$ (%): C 30.69, H 5.22, N 2.32; found: C 30.37, H 5.28, N 2.48.

Characterization of the complex POM-ZnPc in solution

2 mg of POM-pyr (0.67×10^{-3} mmol) were introduced in a 5 mm NMR tube with 150 µL of CD_3CN and 350 µL of $CDCl_3$ and characterized by ^1H NMR (600 MHz). 0.6 mg ($1.04.10^{-3}$ mmol) of ZnPc were then partially solubilized in 30 µL of $CDCl_3$ and added to the NMR tube containing the POM-pyr. The reference tube containing the ZnPc alone was prepared with 0.6 mg of ZnPc in 350 µL of $CDCl_3$ and 150 µL of CD_3CN (added after complete solubilization of the ZnPc in the $CDCl_3$).

For the UV-visible spectroscopy, a saturated solution of ZnPc in dichloromethane was prepared (2 mg of ZnPc in 2 mL of CH_2Cl_2 stirred overnight then filtered lead to a solution of 1.05 mmol·L^{-1}) then diluted to obtain a solution at 7.03×10^{-6} mol·L^{-1} in CH_2Cl_2, from which 2 mL were taken and introduced in a cuvet. A solution with 2 mg of POM-pyr in 1 mL of acetonitrile was prepared and used to add small aliquots of POMs with successive recording of UV-visible spectra (14 µL of this solution were collected to add one equivalent of POMs in the cuvet). To prepare the blank experiment, the same solution of ZnPc was introduced in a cuvet, and the same volumes of pure acetonitrile were added step by step with successive UV-visible measurements.

Surface sample preparation

The solvents used for surface deposition were carefully taken from new or freshly opened bottles. Chloroform was chosen for the deposition on HOPG for its cleanliness (crucial for AFM-IR) and its higher boiling point (to ensure a slow solvent evaporation that should allow a better organization of the molecules on the surface). A solution of TSB in chloroform (10^{-4} mol·L^{-1}) was prepared and 2×10 µL were drop-casted on a freshly cleaved HOPG substrate, then immediately covered with an inverted watchglass to slow down solvent evaporation. The modified substrate was then directly used for the deposition of ZnPc or the complex POM-ZnPc. For the ZnPc/HOPG sample, 2×10 µL of a ZnPc solution at 1.53×10^{-6} mol·L^{-1} in chloroform (the saturated solution prepared as described above was diluted 686 times in $CHCl_3$). For the POM-ZnPc/HOPG sample, a mixed solution at 1.3×10^{-6} mol·L^{-1} (ZnPc/POM 1:1 in mol) in a mixture of $CH_3CN/CHCl_3$ (30:70 in volume) was first prepared and 2×10 µL were deposited on the TSB modified HOPG substrate.

Characterization techniques

NMR spectroscopy. The NMR spectra were recorded on a Bruker AvanceII 300 MHz spectrometer equipped with a 5 mm QNP probehead (^1H, ^{13}C, ^{31}P, ^{19}F) or a Bruker AvanceIII 600 MHz spectrometer equipped with a 5 mm BBFO probehead. The ^1H-NMR spectra were recorded using a pulse sequence of proton (zg30) with a spectral width of 20 Hz, an acquisition time of 5.45 s and a relaxation decay of 2 s. The ^{31}P-NMR spectrum was recorded with a spectral width of 100 Hz, an acquisition time of 2.69 s and a relaxation decay of 2 s. ^1H chemical shifts are quoted as parts per million (ppm) relative to the solvent signals

(s: singlet, d: doublet, t: triplet, sex: sextet, m: multiplet) and coupling constants (J) are quoted in Hertz (Hz). ^{31}P chemical shifts are quoted relative to 85% H_3PO_4. The spectra were analyzed with MestreNova 14.2.

Infrared spectroscopy. The powder spectra were recorded from a KBr pellet on a Jasco FT/IR 4100 spectrometer.

UV-visible spectroscopy. UV visible spectra were recorded on an Agilent Cary 5000, with a 1 cm cuvet.

High resolution mass spectrometry. ESI-MS experiments were recorded using an LTQ Orbitrap hybrid mass spectrometer (Thermofisher Scientific, Bremen, Germany) equipped with an external ESI source operated in the negative ion mode. Spray conditions included a spray voltage of 3.5 kV, a capillary temperature maintained at 270 °C, a capillary voltage of −40 V, and a tube lens offset of −100 V. Sample solutions in acetonitrile (10 pmol·μL^{-1}) were infused into the ESI source by using a syringe pump at a flow rate of 180 μL.h^{-1}. Mass spectra were acquired in the Orbitrap analyzer with a theoretical mass resolving power (R_p) of 100,000 at m/z 400, after ion accumulation to a target value of 10^5 and a m/z range detection from m/z 300 to 2000. All data were acquired using external calibration with a mixture of caffeine, MRFA peptide and Ultramark 1600 dissolved in Milli-Q water/ HPLC grade acetonitrile (50/50, v/v).

Elemental analyses. Elemental analyses were performed at the Institut de Chimie des Substances Naturelles, Gif sur Yvette, France.

Scanning tunneling microscopy. All experiments were performed using 5100 AFM/SPM microscope system equipped with Keysight 1 μm STM scanner. STM images were recorded in constant current mode, at air-solid interface and room temperature using mechanically cut Pt/Ir (80/20) tips (GoodFellow, UK). The tip-sample bias voltage was kept between - 1700 and - 1000 mV and the tunneling current setpoint between 10 and 16 pA. All experiments were repeated several times with different tips, at different spots on the sample, and the results presented in this article are representative and consistent with the more comprehensive data set. STM images were treated and analyzed using the WSxM software.

Raman spectroscopy. Raman experiments were performed on a HR800 and an Infinity from HORIBA with excitation wavelength $\lambda_0 = 458$ nm and $\lambda_0 = 633$ nm, respectively. Both spectrometers were coupled with confocal microscope using a x100 objective giving a spot size at the focus point of around 1 μm in diameter. The illumination power at the focus point was fixed at 30 μW. Careful attention was paid to measure exactly the same aggregates with the two Raman setups used. Time of integration was between 30 and 60 s and an average of 3 spectra was done for each measurement.

Infrared absorption nanospectroscopy. The AFM-IR system was a Dimension IconIR from Bruker with an infrared tunable QCL laser from Daylight Solutions covering the 1900–900 cm^{-1} range. The pulse length was fixed at 100 ns for all the experiments. The cantilever used for Tapping AFM-IR was from NanoSensors reference PPP-NCHAu-MB-10 where the first tapping mode was centered around 280 kHz used for IR signal and the second mode around 1.6 MHz used for the tapping drive. The tip was a sharp silicon tip covered by gold, with a radius estimated below 50 nm. Speed of scan was fixed to 0.3 Hz for each analysis. On all the spectra presented in this article, two bands appeared systematically at 1100 and 1740 cm^{-1}. They may be due to the detection of traces of silicone oils used for the manufacturing of the tip cantilever under local heating during the absorption process.

DFT calculations

DFT calculations were performed using the Gaussian16 suite of programs. The results were visualized by GaussView. Initially, the structure was optimized using the B3LYP functional[41,42] and 6–31 g(d) basis set. Frequency calculation on the optimized structure revealed no imaginary frequencies, verifying that the optimized structure corresponds to an absolute minimum. IR spectra were traced with a scaling factor of 0.96[43,44] using GaussSum[45].

Data availability

The datasets generated during and/or analysed during the current study are available from the corresponding author on reasonable request.

Received: 28 August 2024; Accepted: 3 December 2024;
Published online: 19 December 2024

References

1. Avinash, M. B. & Govindaraju, T. Architectonics: design of molecular architecture for functional applications. *Acc. Chem. Res.* **51**, 414–426 (2018).
2. Zhang, L., Wang, N. & Li, Y. Design, synthesis, and application of some two-dimensional materials. *Chem. Sci.* **14**, 5266–5290 (2023).
3. Ariga, K. Materials nanoarchitectonics in a two-dimensional world within a nanoscale distance from the liquid phase. *Nanoscale* **14**, 10610–10629 (2022).
4. Yoshimoto, S. & Ogata, H. Molecular planting of a single organothiol into a "gap-site" of a 2D patterned adlayer in an electrochemical environment. *Chem. Sci.* **13**, 4999–5005 (2022).
5. Stähler, C. et al. Highly ordered co-assembly of bisurea functionalized molecular switches at the solid-liquid interface. *Chem. A Eur. J.* e202303994 https://doi.org/10.1002/chem.202303994 (2024)
6. Badami-Behjat, A. et al. Versatile role of molecule–surface interactions for monolayer self-assembly at liquid–solid interfaces: substrate-induced polymorphism, thermodynamic stability, and new polymorphs. *Chem. Mater.* **34**, 8876–8884 (2022).
7. Edmondson, M. et al. Order, disorder, and metalation of tetraphenylporphyrin (2 *H* -TPP) on Au(111). *Chem. Commun.* **58**, 6247–6250 (2022).
8. Aoi, S. et al. Spatially controlled aryl radical grafting of graphite surfaces guided by self-assembled molecular networks of linear alkane derivatives: the importance of conformational dynamics. *Langmuir* **39**, 5986–5994 (2023).
9. Sosa-Vargas, L., Kim, E. & Attias, A.-J. Beyond "decorative" 2D supramolecular self-assembly: strategies towards functional surfaces for nanotechnology. *Mater. Horiz.* **4**, 570–583 (2017).
10. Tobe, Y., Tahara, K. & De Feyter, S. Chirality in porous self-assembled monolayer networks at liquid/solid interfaces: induction, reversion, recognition and transfer. *Chem. Commun.* **57**, 962–977 (2021).
11. Carloni, L., Bezzu, C. G. & Bonifazi, D. Patterning porous networks through self-assembly of programmed biomacromolecules. *Chem. A Eur. J.* **25**, 16179–16200 (2019).
12. Judd, C. J., Champness, N. R. & Saywell, A. An on-surface reaction confined within a porous molecular template. *Chem. A Eur. J.* **24**, 56–61 (2018).
13. Rubio-Giménez, V. et al. High-quality metal–organic framework ultrathin films for electronically active interfaces. *J. Am. Chem. Soc.* **138**, 2576–2584 (2016).
14. Mali, K. S., Pearce, N., De Feyter, S. & Champness, N. R. Frontiers of supramolecular chemistry at solid surfaces. *Chem. Soc. Rev.* **46**, 2520–2542 (2017).
15. Tessari, Z., Rinkovec, T. & De Feyter, S. Chiral induction in substrate-supported self-assembled molecular networks under nanoconfinement conditions. *Nanoscale Adv.* **6**, 892–901 (2024).
16. DelaCruzCalupitan, J. P., Galangau, O., Nakashima, T., Kawai, T. & Rapenne, G. Photochromic diarylethenes designed for surface

deposition: from self-assembled monolayers to single molecules. *ChemPlusChem* **84**, 564–577 (2019).
17. Kim, B. et al. 2D host–guest supramolecular chemistry for an on-monolayer graphene emitting platform. *Mater. Horiz.* **7**, 2741–2748 (2020).
18. Brisse, R. et al. Probing the in-air growth of large area of 3D functional structures into a 2D supramolecular nanoporous network. *Chem. Commun.* **54**, 10068–10071 (2018).
19. Le Liepvre, S. et al. Fluorescent self-assembled molecular monolayer on graphene. *ACS Photon.* **3**, 2291–2296 (2016).
20. Saywell, A. et al. Self-assembled aggregates formed by single-molecule magnets on a gold surface. *Nat. Commun.* **1**, 75 (2010).
21. Fernez, Q. et al. From molecules in solution to molecules on surfaces —using supramolecular dyads to form functional self-assembled networks on graphene. *J. Mater. Chem. C* **10**, 13981–13988 (2022).
22. Dazzi, A., Prazeres, R., Glotin, F. & Ortega, J. M. Local infrared microspectroscopy with subwavelength spatial resolution with an atomic force microscope tip used as a photothermal sensor. *Opt. Lett.* **30**, 2388 (2005).
23. Dazzi, A. & Prater, C. B. AFM-IR: technology and applications in nanoscale infrared spectroscopy and chemical imaging. *Chem. Rev.* **117**, 5146–5173 (2017).
24. Dos Santos, A. C. V. D., Lendl, B. & Ramer, G. Systematic analysis and nanoscale chemical imaging of polymers using photothermal-induced resonance (AFM-IR) infrared spectroscopy. *Polymer Testing* **106**, 107443 (2022).
25. Lu, F., Jin, M. & Belkin, M. A. Tip-enhanced infrared nanospectroscopy via molecular expansion force detection. *Nat. Photon* **8**, 307–312 (2014).
26. Hamadeh, A. et al. Toward conformational identification of molecules in 2D and 3D self-assemblies on surfaces. *Commun. Chem.* **6**, 246 (2023).
27. Stiegler, J. M. et al. Nanoscale infrared absorption spectroscopy of individual nanoparticles enabled by scattering-type near-field microscopy. *ACS Nano* **5**, 6494–6499 (2011).
28. Rosenberger, M. R. et al. Measuring individual carbon nanotubes and single graphene sheets using atomic force microscope infrared spectroscopy. *Nanotechnology* **28**, 355707 (2017).
29. Ruggeri, F. S., Mannini, B., Schmid, R., Vendruscolo, M. & Knowles, T. P. J. Single molecule secondary structure determination of proteins through infrared absorption nanospectroscopy. *Nat. Commun.* **11**, 2945 (2020).
30. Ruggeri, F. S. et al. Infrared nanospectroscopy reveals the molecular interaction fingerprint of an aggregation inhibitor with single Aβ42 oligomers. *Nat. Commun.* **12**, 688 (2021).
31. Custovic, I., Pocholle, N., Bourillot, E., Lesniewska, E. & Piétrement, O. Infrared nanospectroscopic imaging of DNA molecules on mica surface. *Sci. Rep.* **12**, 18972 (2022).
32. Pope, M., Sadakane, M. & Kortz, U. Special Issue. Celebrating Polyoxometalates. *Eur. J. Inorg. Chem.* **2019**, 336–541 (2019).
33. Moors, M. et al. Insights from adsorption and electron modification studies of polyoxometalates on surfaces for molecular memory applications. *Acc. Chem. Res.* **54**, 3377–3389 (2021).
34. Matt, B. et al. Elegant approach to the synthesis of a unique heteroleptic cyclometalated iridium(III)-polyoxometalate conjugate. *Organometallics* **31**, 35–38 (2012).
35. Rinfray, C., Renaudineau, S., Izzet, G. & Proust, A. A covalent polyoxomolybdate-based hybrid with remarkable electron reservoir properties. *Chem. Commun.* **50**, 8575–8577 (2014).
36. Basolo, F., Jones, R. D. & Summerville, D. A. Equilibrium constants for the axial coordination of meso-tetraphenylporphinatomanganese(II) and chromium(III) complexes. *Acta Chem. Scand. A* **32**, 771–780 (1978).
37. Arrigoni, C. et al. Structure and epitaxial registry on graphite of a series of nanoporous self-assembled molecular monolayers. *J. Phys. Chem. Lett.* **1**, 190–194 (2010).
38. Leng, W. & Myers Kelley, A. Resonance hyper-Raman spectra of zinc phthalocyanine. *J. Phys. Chem. A* **112**, 5925–5929 (2008).
39. Salhi, J. et al. Ready-to-be-addressed oxo-clusters: individualized, periodically organized and separated from the substrate. *Nanoscale* **15**, 13233–13238 (2023).
40. Rocchiccioli-Deltcheff, C & Thouvenot, R. Metal complexes of heteropolyanions a-XM11O39n- with X= Si(IV) or P(V) and M=Mo(VI) or W(VI): study of structural modifications of ligands by infrared and Raman spectrometry. *J. Chem. Res.,* 46–47 (1977).
41. Becke, A. D. Density-functional thermochemistry. III. The role of exact exchange. *J. Chem. Phys.* **98**, 5648–5652 (1993).
42. Stephens, P. J., Devlin, F. J., Chabalowski, C. F. & Frisch, M. J. Ab initio calculation of vibrational absorption and circular dichroism spectra using density functional force fields. *J. Phys. Chem.* **98**, 11623–11627 (1994).
43. Gong, X. D., Xiao, H. M. & Tian, H. Comparative studies on the structures, infrared spectrum, and thermodynamic properties of phthalocyanine using ab initio Hartree–Fock and density functional theory methods. *Int. J. Quant. Chem.* **86**, 531–540 (2002).
44. Wong, M. W. Vibrational frequency prediction using density functional theory. *Chem. Phys. Lett.* **256**, 391–399 (1996).
45. O'boyle, N. M., Tenderholt, A. L. & Langner, K. M. cclib: a library for package-independent computational chemistry algorithms. *J. Comput. Chem.* **29**, 839–845 (2008).

Acknowledgements

We acknowledge support of the Ville de Paris (grant *Emergence 2019 DAE 81*) and National Research Agency (*France 2030, "ANR-22-EXSP-0007"*). The authors acknowledge Digital Surf for Mountains Map software support. This work was supported by the Paris Ile-de-France Region-DIM "Matériaux anciens et patrimoniaux". J.P.C. acknowledges Marie Skłodowska-Curie Actions Postdoctoral Fellowship Grant Agreement No. 101153230.

Author contributions

J.S. and M.M. contributed equally and developed the synthesis of the POM-pyr and POM-ZnPc complex, their characterizations, their deposition on HOPG and STM characterization, and followed all the advanced surface characterizations. J.P.C. performed the DFT calculations. F.V., A.P., and G.I. supervised the syntheses. I.A. supervised the STM experiments. C.T. supervised the NMR experiments. S.A. performed the ESI-MS experiments. G.S. and C.P. performed the Raman spectroscopy experiments. A.D. performed and supervised all the AFM-IR experiments. F.V., I.A., and D.K. conceived the project. F.V. coordinated all the project. The manuscript was written by F.V. through contributions of all authors. All authors have given approval to the final version of the manuscript.

Competing interests

The authors declare no competing interests.

Additional information

Supplementary information The online version contains supplementary material available at https://doi.org/10.1038/s42004-024-01385-y.

Correspondence and requests for materials should be addressed to Florence Volatron.

Peer review information *Communications Chemistry* thanks Georg Ramer and the other, anonymous, reviewer for their contribution to the peer review of this work. Peer reviewer reports are available.